AIP | Physics of Plasmas

Magnetic stochasticity and transport due to nonlinearly excited subdominant microtearing modes

D. R. Hatch, M. J. Pueschel, F. Jenko, W. M. Nevins, P. W. Terry et al.

Citation: Phys. Plasmas **20**, 012307 (2013); doi: 10.1063/1.4789448
View online: http://dx.doi.org/10.1063/1.4789448
View Table of Contents: http://pop.aip.org/resource/1/PHPAEN/v20/i1
Published by the AIP Publishing LLC.

Additional information on Phys. Plasmas

Journal Homepage: http://pop.aip.org/
Journal Information: http://pop.aip.org/about/about_the_journal
Top downloads: http://pop.aip.org/features/most_downloaded
Information for Authors: http://pop.aip.org/authors

ADVERTISEMENT

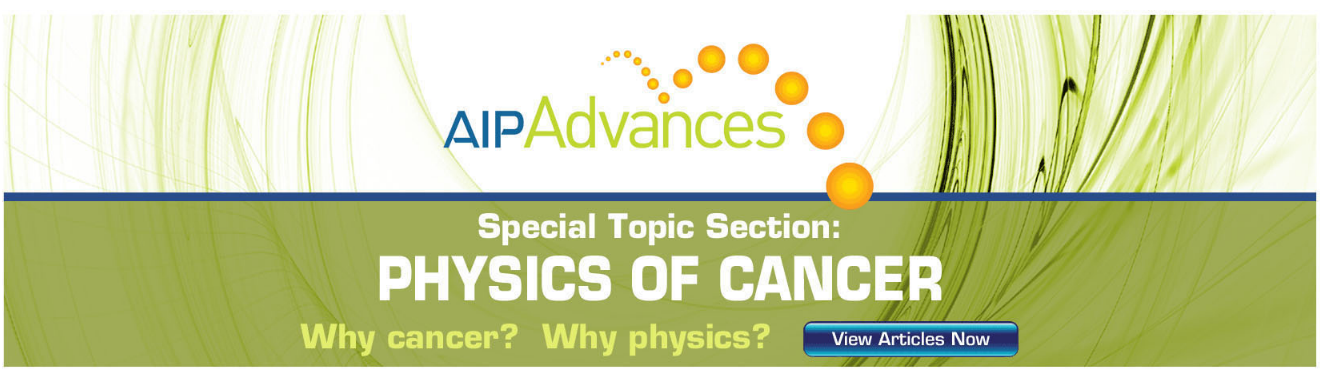

Downloaded 07 Aug 2013 to 130.183.100.98. This article is copyrighted as indicated in the abstract. Reuse of AIP content is subject to the terms at: http://pop.aip.org/about/rights_and_permissions

Magnetic stochasticity and transport due to nonlinearly excited subdominant microtearing modes

D. R. Hatch,[1] M. J. Pueschel,[2] F. Jenko,[1] W. M. Nevins,[3] P. W. Terry,[2] and H. Doerk[1]
[1]*Max-Planck-Institut für Plasmaphysik, EURATOM Association, 85748 Garching, Germany*
[2]*University of Wisconsin-Madison, Madison, Wisconsin 53706, USA*
[3]*Lawrence Livermore National Laboratory, Livermore, California 94550, USA*

(Received 12 October 2012; accepted 27 December 2012; published online 31 January 2013)

Subdominant, linearly stable microtearing modes are identified as the main mechanism for the development of magnetic stochasticity and transport in gyrokinetic simulations of electromagnetic ion temperature gradient driven plasma microturbulence. The linear eigenmode spectrum is examined in order to identify and characterize modes with tearing parity. Connections are demonstrated between microtearing modes and the nonlinear fluctuations that are responsible for the magnetic stochasticity and electromagnetic transport, and nonlinear coupling with zonal modes is identified as the salient nonlinear excitation mechanism. A simple model is presented, which relates the electromagnetic transport to the electrostatic transport. These results may provide a paradigm for the mechanisms responsible for electromagnetic stochasticity and transport, which can be examined in a broader range of scenarios and parameter regimes. © *2013 American Institute of Physics*. [http://dx.doi.org/10.1063/1.4789448]

I. INTRODUCTION

The influence of electromagnetic (EM) effects on confinement in fusion plasmas is still an open question. EM effects allow magnetic fluctuations to evolve self-consistently with other turbulent fluctuations, providing an additional transport mechanism: radial heat flux via electrons streaming along perturbed field lines. EM effects may be parameterized by $\beta = 8\pi n_e T_e / B_{\rm ref}^2$, which quantifies the degree to which magnetic fluctuations can participate in plasma dynamics. Experimentally, the scaling of confinement with β varies widely depending on the device–notably both ASDEX Upgrade and JT-60U exhibit unfavorable beta scaling.[1] Thus, extrapolation to ITER is uncertain—a critical gap in our understanding, considering that ITER is expected to operate at high β. In this study, we use the gyrokinetic GENE code[2] to examine in detail the mechanisms by which magnetic stochasticity and EM transport arise in turbulent systems driven by instabilities, which are not intrinsically electromagnetic (e.g., ion temperature gradient (ITG)[3,4] driven and trapped electron mode (TEM)[5–7] turbulence). This paper expands on the results reported in Ref. 8.

In the past decade, several studies have explored EM effects in the context of gyrokinetic simulations.[2,8–18] A series of these studies[8,12–18] has been based on a finite-β variation of the cyclone base case (CBC)[4] parameters. The CBC is likely the most-studied gyrokinetic turbulence scenario and has served as a basic paradigm for toroidal turbulent transport dynamics for over a decade. Thus, studies of an electromagnetic variation of this case can be considered to provide intuition into the most fundamental ways in which EM effects modify basic paradigms of turbulent transport. Such studies have shown that the growth rate of the ITG mode decreases gradually as β increases, while the corresponding electrostatic (ES) transport levels decrease somewhat more sharply.[14] The EM transport level, in contrast, increases with a β^2 dependence and at moderate to high β can become comparable to the ES transport channels. The behavior of this EM transport contrasts sharply with the quasilinear expectations derived from the linear ITG mode: the linear ITG mode defines an inward EM heat flux, which scales like β, whereas a robustly outward β^2 scaling is observed in the nonlinear simulations. In Refs. 17 and 18, this transport has been linked to magnetic stochasticity, which is evident even at very low values of β. This stochasticity is somewhat puzzling in light of the fact that the ITG mode is characterized by ballooning parity (antisymmetric $A_{||}$ parallel mode structures about the outboard midplane), and not tearing parity (symmetric $A_{||}$ mode structures), and is thus poorly equipped for breaking magnetic field lines (for a more nuanced discussion see Sec. II B). Thus, one might naively expect very limited impact of the magnetic fluctuations from ITG driven turbulence on the field line topology and EM transport. The present study resolves these contradictions by demonstrating that the magnetic stochasticity and associated transport are *not* caused directly by the driving ITG mode. Rather, the salient mechanism is linearly stable microtearing modes (MTMs),[19–30] which are driven nonlinearly and operate at the same perpendicular scales as the ITG modes. Nonlinear coupling with zonal modes (modes at $k_y = 0$, a definition broad enough to encompass both zonal flows and geodesic acoustic modes (GAMs)[31]) is shown to be the responsible excitation mechanism. These results provide an explanation for many of the EM effects observed in Refs. 12, 14, 15, 17, and 18 and offer a paradigm for EM transport, which can be explored more extensively throughout parameter space in future studies.

In order to further place this work in context, we briefly review two related threads of research. Microtearing modes—small-scale variants of MHD tearing modes—are electromagnetic (they exhibit a β threshold and intrinsically depend on magnetic fluctuations) modes that are driven by

1070-664X/2013/20(1)/012307/12/$30.00 © 2013 American Institute of Physics

Downloaded 07 Aug 2013 to 130.183.100.98. This article is copyrighted as indicated in the abstract. Reuse of AIP content is subject to the terms at: http://pop.aip.org/about/rights_and_permissions

electron temperature gradients (ETGs). Early theoretical predictions[22] suggested that MTMs would be stable in standard-aspect-ratio tokamaks, leading to the expectation that such devices would be unaffected by microtearing physics. Recently, however, it has been shown that MTMs can be linearly unstable[29,30] and nonlinearly produce experimentally relevant heat fluxes.[24] Here, we show that even when MTMs are completely stable linearly, they can be excited nonlinearly and produce significant levels of transport.

This study also extends and builds upon a body of work that has explored the role of subdominant eigenmodes in plasma microturbulence. Subdominant damped modes facilitate turbulent saturation by offering an energy sink at the same scales as the driving instabilities—via inward transport in fluid models[32–34] and collisional dissipation in gyrokinetic systems.[35,36] In another scenario, subdominant *unstable* modes have been shown to coexist nonlinearly and compete with the dominant instabilities in mixed ITG and TEM regimes.[37] In this paper, we illustrate a situation where different transport channels are activated by physically distinct processes—the ES transport is driven by the dominant ITG instability, while the electron EM transport is caused by the nonlinear excitation of subdominant tearing modes.

The remainder of this paper is outlined as follows: In Sec. II, we describe the numerical and physical parameters used for the GENE simulations and introduce the parity considerations for field-following coordinates with relation to magnetic-field-line-breaking and stochasticity. In Sec. III, we demonstrate that tearing-parity fluctuations are responsible for the magnetic stochasticity and transport and eliminate the ITG mode as the primary mechanism. In Sec. IV, we describe and characterize the tearing-parity modes in the linear eigenmode spectrum. Three classes of such modes are identified: tearing-parity variants of ITG and ETG[2,38,39] modes, and a subdominant, linearly stable MTM. In Sec. V, we compare various aspects of the nonlinear fluctuations with the linear eigenmodes described in Sec. IV, and conclude that the MTM is indeed responsible for the EM effects of interest. In Sec. VI, we demonstrate that the EM transport is nonlinearly driven and that the excitation mechanism is nonlinear coupling with zonal modes. In Sec. VII, we describe a model relating the EM transport to the ES transport and discuss how EM effects are expected to be manifest throughout a broader range of parameters. A summary and conclusions are provided in Sec. VIII.

II. DESCRIPTION OF SIMULATIONS AND PARITY CONSIDERATIONS

A. Physical and numerical description of simulations

This study uses the GENE code to examine EM gyrokinetic simulations based on an EM variant of the CBC parameters: normalized density gradient scale length, $R/L_n = 2.22$, ion and electron temperature gradient scale lengths, $R/L_{Ti,e} = 6.89$, magnetic shear $\hat{s} = 0.79$, safety factor $q_0 = 1.4$, inverse aspect ratio $\epsilon_t = 0.18$, and β covering points from the ES limit ($\beta = 1.0 \times 10^{-4}$) to values approaching the kinetic ballooning mode (KBM) threshold $\beta_{\rm crit}$ (in this case, $\beta_{\rm crit} \approx 0.013$). The simulations use an s-α equilibrium (with $\alpha = 0$) and the local flux tube approximation, which allows for a Fourier representation in the radial ($x \to k_x$) and binormal ($y \to k_y$) directions, which are both perpendicular to the background magnetic field. The coordinate z along the magnetic field corresponds to the poloidal angle. The numerical grid resolves a $z = [-\pi, \pi)$ domain, which is effectively extended along the field line by applying the flux tube parallel boundary condition,[40] $f_{k_x,k_y}(z = \pi) = (-1)^{\Delta k_x/k_x^{min}} f_{k_x+\Delta k_x,k_y}(z = -\pi)$, where $\Delta k_x = 2\pi\hat{s}k_y$ and k_x^{min} is the minimum radial wave number. The extended parallel structure of the fluctuations can be recovered by connecting all k_x modes, which are linked by this boundary condition. In this paper, we will call this collection of connected k_x modes the *extended mode structure* or often simply *mode structure* and will denote as k_x^+ all k_x modes comprising an extended mode structure. The two-dimensional gyrokinetic velocity space is covered by the parallel velocity $v_{||}$ and the magnetic moment μ. The nominal perpendicular spatial resolution consists of 192 k_x modes with $k_x^{min}\rho_s = 0.062$ (covering positive and negative wave numbers), and 24 k_y modes with $k_y^{min}\rho_s = 0.05$ (covering $k_y = [0, k_y^{max}]$, with the negative wave numbers implicitly determined by the reality constraint). Here, ρ_s is the ion sound radius. The resolution in the $(z, v_{||}, \mu)$ coordinates is $(24, 48, 8)$, respectively, with simulations at higher β often extending to 48 z grid points. Fourth order hyperdiffusion (as described in Ref. 41) is applied in the k_x, z, and $v_{||}$ coordinates with coefficients of (0.2, 8.0, and 0.2) respectively. The parallel hyperdiffusivity is often reduced in more recent simulations, which use an Arakawa[42] scheme for the parallel spatial and velocity coordinates.

Much of the data used in this study are taken from the dataset described in Ref. 14. ITG is the dominant instability through a large portion of this scan (up to $\beta \sim 0.01$), above which TEM becomes the dominant linear instability until the KBM limit is reached. The simulations above $\beta \sim 0.008$ are only transiently saturated before a delayed transition to extremely high transport levels, as described in Refs. 16 and 43. Additional parameter regimes, including a TEM β scan[15] and a collisionality scan, are also discussed and will be described below.

B. Parity considerations

Magnetic stochasticity is caused by the overlap of magnetic islands, which can form when a magnetic perturbation aligns with the background magnetic field at a mode-rational q-surface. In toroidal coordinates, this resonance condition is well-known: $q_{res} = m/n$, where m is the poloidal mode number and n is the toroidal mode number. In the field-aligned coordinate system used here, the parallel z coordinate labels the distance along the field line (and corresponds to the poloidal angle), and the binormal coordinate $y = \varphi - q(x)z$ depends on both the toroidal φ and poloidal z angles. In this representation, the resonance condition must be expressed differently, now as the requirement that the integral along the field line of the parallel magnetic vector potential be non-vanishing at a mode-rational flux surface,

$$A_{||}^{res} = \int A_{||}(x = x_{res}(k_y), k_y, z)dz\,, \qquad (1)$$

Downloaded 07 Aug 2013 to 130.183.100.98. This article is copyrighted as indicated in the abstract. Reuse of AIP content is subject to the terms at: http://pop.aip.org/about/rights_and_permissions

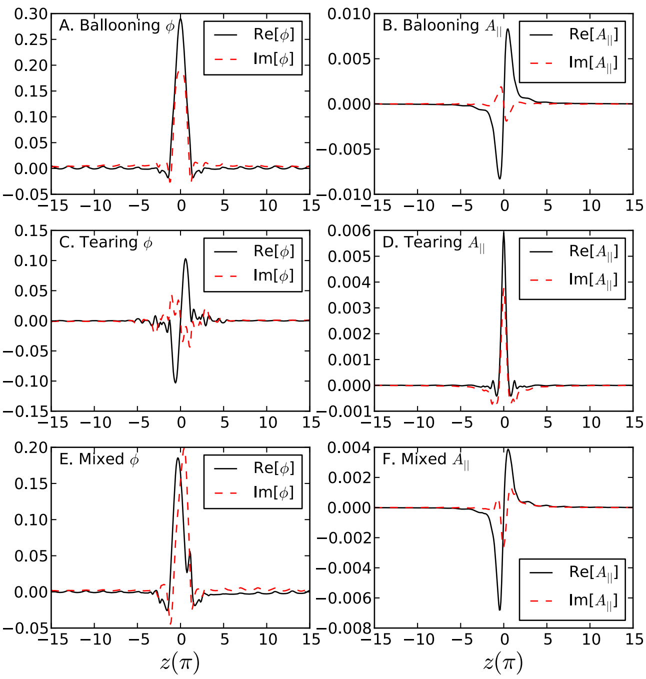

FIG. 1. Extended parallel mode structures representative of ballooning parity ((A) and (B)), tearing parity ((C) and (D)), and mixed parity ((E) and (F)). The mixed-parity mode is an ITG mode centered at $k_x\rho_s = 0.124$.

where the z domain covers the extended mode structure. As a result of this resonance condition, a mode with ballooning parity (odd parity about the outboard midplane $z = 0$) can never be resonant, while a mode with tearing (even) parity can (and typically will) be resonant. More generally, these parity considerations can be extended to the underlying distribution function from which $A_{||}$ is derived: considering only the parallel velocity and parallel coordinate, the condition $g(z, v_{||}) = g(-z, -v_{||})$ defines ballooning parity and produces an even electrostatic potential Φ mode structure and an odd $A_{||}$ mode structure (as seen in Figs. 1(A) and 1(B)), while the condition $g(z, v_{||}) = -g(-z, -v_{||})$ defines tearing parity and produces an odd Φ mode structure and an even $A_{||}$ mode structure (as seen in Figs. 1(C) and 1(D)). For an up-down symmetric equilibrium at $k_x = 0$, the gyrokinetic equations enforce one or the other of these parities on all eigen-solutions of the linear operator. The most familiar microinstabilities (including the ITG mode, TEM, ETG mode, and KBM) are characterized by ballooning parity.

At finite radial wave numbers, the parity is no longer enforced, and the linear eigenmodes can be characterized by mixed parity. Nevertheless, the natural parity of the mode is still predominant, as is seen in a representative example for the ITG mode shown in Figs. 1(E) and 1(F).

Thus, the candidate mechanisms for producing magnetic stochasticity and the associated transport are (1) the small tearing component of $|k_x| > 0$ ITG modes, and (2) some other mode entirely, which is characterized by tearing parity. In the following sections, we demonstrate that the latter is the predominant mechanism in the form of linearly stable, nonlinearly excited MTMs.

III. CONNECTING PARITY, STOCHASTICITY AND TRANSPORT IN NONLINEAR SIMULATIONS

A. Tearing-ballooning decomposition

In this section, we characterize the $A_{||}$ fluctuations that contribute to the nonlinear dynamics in order to identify what kinds of fluctuations are responsible for the stochasticity and transport. To this end, we seek to decompose the magnetic fluctuations into classes corresponding to the parity considerations described in Sec. II B. In principle, the magnetic field can be decomposed into an even and an odd component for every wave number in the system. However, this would not account for the extended mode structure of the fluctuations and would fail to distinguish finite k_x ITG modes (which have mixed parity) from legitimate tearing-parity modes. We thus construct a decomposition, which naturally reflects the inherent structures of the nonlinear fluctuations without externally enforcing any parity constraints. This is accomplished by constructing singular value decompositions (SVDs)[44] of the magnetic vector potential fluctuations. In this application, SVDs are constructed from matrices whose columns consist of extended $A_{||}$ mode structures; i.e., each column of the input matrix is a time point of the nonlinearly evolved $A_{||}$ mode structure. This produces a decomposition of the form

$$A_{||k_x^+,k_y}(z,t) = \sum_n A^{(n)}_{||k_x^+,k_y}(z) h^{(n)}_{k_x^+,k_y}(t), \tag{2}$$

where $A^{(n)}_{||}$ is called the nth SVD mode, and the SVD time amplitude $h^{(n)}(t)$ defines the time dependent amplitude of the nth SVD mode such that the superposition exactly reproduces the nonlinear fluctuations at each moment in time (note that in this representation, the singular values are subsumed in the time amplitudes $h^{(n)}(t)$). Both the spatial and temporal SVD modes are orthogonal and optimal in the sense that a truncation of the decomposition rigorously captures the dynamics (as quantified by the $|A_{||}|^2$ fluctuation intensity) better than any other decomposition of the same rank. Because of this property, the decomposition can be considered to extract the most important features of the fluctuations in the fewest possible number of modes.

When SVDs are constructed from the nonlinear mode structures, the first two SVD modes almost invariably define a clear ballooning component and a clear tearing component. An example is shown in Fig. 2, where the $n = 1$ and $n = 2$ modes are plotted for $k_y\rho_s = 0.2, k_x\rho_s = 0$, and $\beta = 0.003$. In the nonlinear fluctuations, these two modes are superimposed according to their time amplitudes $h^{(n)}(t)$ such that the full nonlinear mode structure can exhibit mixed parity and alternate between periods of dominant tearing parity and dominant ballooning parity. As will be shown, nearly all of the important effects of the magnetic fluctuations can be captured with only these two modes (i.e., the first two SVD modes for each wave number).

When the k_x value is non-zero, the modes may peak at the corresponding non-zero ballooning angle and also exhibit some mixing of the parity in a fashion similar to that observed in the linear modes (as described in Sec. II B). Even in these cases, there typically remains one mode, which is predominantly tearing and one which is predominantly ballooning. In

Downloaded 07 Aug 2013 to 130.183.100.98. This article is copyrighted as indicated in the abstract. Reuse of AIP content is subject to the terms at: http://pop.aip.org/about/rights_and_permissions

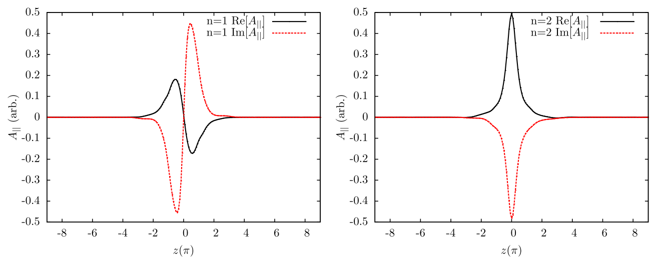

FIG. 2. The first two parallel mode structures extracted by an SVD decomposition of $A_{||}$ at $k_y\rho_s = 0.2$ and centered at $k_x\rho_s = 0$. The $n=1$ mode (left) has ballooning parity, and the $n=2$ mode (right) has tearing parity. Reprinted with permission from D. R. Hatch *et al.*, Phys. Rev. Lett. **108**, 235002 (2012). Copyright 2012 the American Physical Society.

order to automatically distinguish the ballooning components from the tearing components, a parity factor is defined

$$P = \frac{\left|\int dz A_{||}\right|}{\int dz \left|A_{||}\right|}. \tag{3}$$

The parity factor is zero for pure ballooning parity and may be as high as one for tearing parity modes. By constructing SVDs of each (k_x^+, k_y) and applying this parity factor, a tearing-ballooning decomposition of the entire $A_{||}$ dataset can be constructed as follows:

$$A_{||_{k_x,k_y}}(k_x, k_y, z, t) = A^{(ball)}_{||_{k_x,k_y}}(z,t) + A^{(tear)}_{||_{k_x,k_y}}(z,t) + A^{(res)}_{||_{k_x,k_y}}(z,t), \tag{4}$$

where the ballooning component (*ball*) is defined as whichever of the first two SVD modes has the smaller parity factor, the tearing component (*tear*) is whichever of the first two SVD modes has the larger parity factor, and the rest of the SVD modes are grouped into the residual (*res*) category.

Note that the parity factor can distinguish between the mixed parity modes at $|k_x| > 0$. For example, consider two modes at the same $|k_x| > 0$ wave number—one which corresponds to the ITG mode and has predominantly ballooning parity, and another which represents a subdominant tearing mode and has predominantly tearing parity. Each mode can be decomposed into an even part and an odd part: $A_{||}(z) = A_{||}^{even} + A_{||}^{odd}$. If the predominantly ballooning-parity mode has a high enough relative amplitude, its even (tearing) component could conceivably dominate that of the predominantly tearing-parity mode and thus be the mechanism for the magnetic stochasticity. Using the parity factor described here, this analysis can distinguish between the fluctuations associated with the dominant ITG modes and the tearing modes and group them appropriately.

This analysis procedure can be summarized as follows: (1) Select a k_y wave number and a k_x^+ extended mode structure from the $A_{||}$ fluctuation data. (2) Construct an SVD of this data set. (3) Select from the first two SVD modes, the one with the largest parity factor and group it in the tearing component of the decomposition. (4) Select from the first two SVD modes the one with the smaller parity factor and group it in the ballooning component of the decomposition. (5) Repeat steps (1)–(4) for all extended mode structures in the dataset. The result is a decomposition (with the form of Eq. (4)) of the entire $A_{||_{k_x,k_y}}(z,t)$, which defines a dominant ballooning component, a dominant tearing component, and all other residual fluctuations.

Now, with this tearing-ballooning decomposition in hand, we can study the contribution of each component to the magnetic field fluctuations and transport as will be done in Sec. III B.

B. Stochasticity and transport from tearing parity fluctuations

Using the decomposition from Eq. (4), we can study the structure of the magnetic field produced by the different modes. In order to do this, a routine is used to follow the trajectory of magnetic field lines and track their deviation from the equilibrium field. This can be quantified with a magnetic diffusivity[17,45]

$$D_{fl} = \lim_{l\to\infty} \langle [r_i(l) - r_i(0)]^2 \rangle / l. \tag{5}$$

Fig. 3 shows the magnetic diffusivities for the different components of the magnetic field. The tearing component of $A_{||}$ produces a magnetic diffusivity that is comparable to the diffusivity produced by the total $A_{||}$ across the β scan, while the ballooning and residual components produce comparatively negligible diffusivities. This demonstrates that the tearing structures, rather than the finite-k_x ITG modes, are responsible for the stochasticity. What has been quantified by the magnetic diffusion coefficient can also be seen intuitively by constructing Poincaré plots (not shown) of the magnetic field lines produced by the different classes of magnetic fluctuations; the tearing component is visibly more stochastic than the ITG and residual components.

The tearing-ballooning decomposition can also be used to directly calculate the contribution of each parity class to the electron EM heat transport $Q_e^{EM} = \langle q_{e||} B_x \rangle / B_{\text{ref}}$, where $\langle\cdot\rangle$ denotes a spatial average, $q_{e||}$ is the parallel electron heat flux moment, and $B_x = ik_yA_{||}$ is the radial component of the

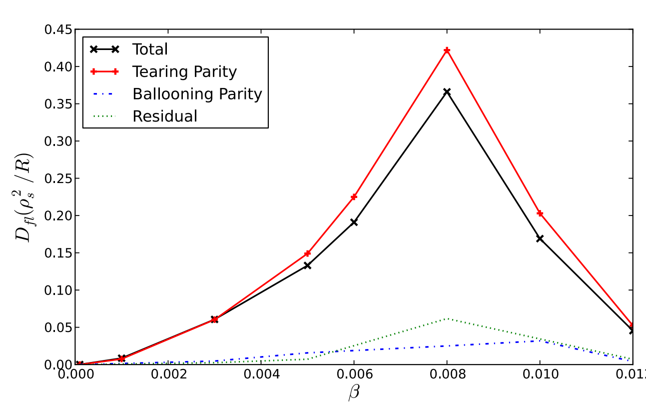

FIG. 3. The magnetic diffusivity associated with different components (defined in Eq. (4)) of the magnetic fluctuations. The magnetic diffusivity associated with the tearing component is comparable to the total magnetic diffusivity, indicating that tearing-parity modes rather than ITG modes are responsible for the magnetic stochasticity.

Downloaded 07 Aug 2013 to 130.183.100.98. This article is copyrighted as indicated in the abstract. Reuse of AIP content is subject to the terms at: http://pop.aip.org/about/rights_and_permissions

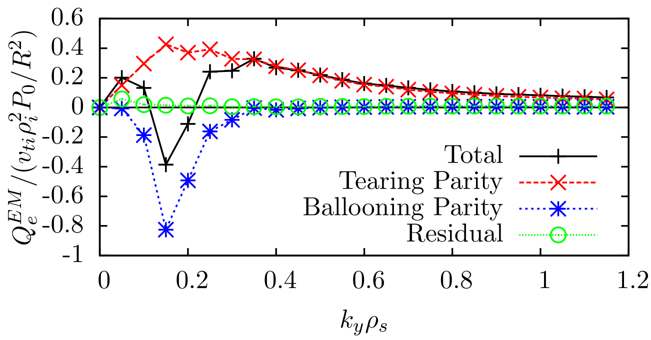

FIG. 4. The k_y-spectra of the electron electromagnetic heat flux associated with different components of the magnetic fluctuations (defined in Eq. (4)). The flux associated with tearing-parity modes is robustly outward, while the flux associated with ballooning parity modes (ITG) is inward and limited to the low-k_y region. The superposition reproduces the net spectrum. Reprinted with permission from D. R. Hatch *et al.*, Phys. Rev. Lett. **108**, 235002 (2012). Copyright 2012 the American Physical Society.

fluctuating magnetic field. The k_y spectra for Q_e^{EM} are quite distinctive (see, e.g., Fig. 6(b) in Ref. 13); they exhibit a dip in the flux at the same scales where the electrostatic transport Q^{ES} peaks ($0.1 \lesssim k_y\rho_s \lesssim 0.3$). This dip dominates at low β and becomes less prominent as β increases. The present analysis shows that this feature is the result of the superposition of the transport associated with the ITG modes and the transport associated with the subdominant tearing modes, as described below.

Using the decomposition defined in Eq. (4), one can define a ballooning component of the flux $\langle q_{e||}B_x^{ball}\rangle/B_{\rm ref}$, a tearing component $\langle q_{e||}B_x^{tear}\rangle/B_{\rm ref}$, and the residual $\langle q_{e||}B_x^{res}\rangle/B_{\rm ref}$. Note that in these expressions, B_x has been decomposed into the different classes of magnetic fluctuations, but the parallel heat flux $q_{e||}$ is the total fluctuating quantity. The k_y flux spectra (at $\beta = 0.003$) for the different components are shown in Fig. 4. The ballooning component of the flux (green plus signs) defines a heat pinch that peaks in the low-k_y region where the ITG modes dominate. In contrast, the tearing component of the transport (red asterisks) is outward, also peaking at low k_y, but additionally extending with significant amplitude to the higher wave numbers in the spectrum. The total transport spectrum is a superposition of these two components. For the $\beta = 0.003$ value shown here, they are similar in magnitude. The ballooning part follows roughly the quasilinear expectation, scaling like β. The tearing component follows a β^2 dependence up to $\beta \approx 0.008$ (a more detailed discussion of this β dependence is provided in Sec. VII) and thus dominates as β increases. This β^2 dependence can also be seen in Fig. 3.

In order to further elucidate the components of the transport, we express the parallel heat flux in terms of the parallel temperature gradient along a perturbed field line[9]

$$q_{e||} = -n_{e0}\chi_{e||}\left(\frac{d\tilde{T}_{e||}}{dz} + \frac{B_x}{B_{\rm ref}}\frac{d\tilde{T}_{e||}}{dx} + \frac{B_x}{B_{\rm ref}}\frac{dT_{e0}}{dx}\right), \qquad (6)$$

where n_{e0} is the electron density, and $\chi_{e||}$ is the parallel electron heat conductivity. As described in Ref. 14, the ITG modes mainly contribute via the first term, which scales like β, while the third term is closely related to the field line diffusivity D_{fl} and describes the heat transport due to streaming along stochastic field lines. The latter is produced by the tearing structures and dominates at high β.

IV. TEARING-PARITY MODES IN THE LINEAR EIGENMODE SPECTRUM

In Sec. III B, we demonstrated that the magnetic stochasticity and transport are associated with tearing-parity fluctuations. In this section, we examine and classify modes with tearing parity in the linear eigenmode spectrum—i.e., the candidates in the linear spectrum for explaining the EM effects described above. To this end, GENE is run as an eigenmode solver in order to resolve subdominant tearing-parity modes. Two solution methods are applied—an iterative solver (based on the SLEPc[46,47] library), which is suitable for finding several eigenmodes in a targeted portion of the spectrum, and a direct solver (based on the SCALAPACK library[48]), which solves for the entire eigenmode spectrum.

Several of the least-damped eigenmodes can be accessed with the iterative SLEPc solver (up to several dozen). These modes range from weakly damped modes to the robustly unstable ITG mode (or TEMs and KBMs, depending on parameters). The modes are quite evenly distributed between the two parity classes, but in all cases observed, the most unstable mode is characterized by ballooning parity. The tearing-parity modes can be further classified in two categories which we call tearing-ITG (TITG) and tearing-ETG (TETG) modes. These names are used because, with the exception of the parity, many other relevant mode properties are identical to the conventional ITG and ETG modes, respectively; as outlined in Table I, the TITG (TETG) modes match the ITG (ETG) modes in the drift direction (i.e., the sign of the frequency), threshold behavior with respect to temperature gradients, and various electromagnetic properties. Notably, none of these modes are intrinsically electromagnetic, i.e., the modes have extremely weak dependence on β and are largely unchanged in the $\beta \to 0$ limit. Representative TITG and TETG mode structures are shown in Fig. 5—notable features include the distinctive extended $A_{||}$ mode structure of the TETG mode (seen in (C) and (D)) and the lobes of the TITG $A_{||}$ mode, which change sign at approximately $z = \pm\pi$ (seen in (B)). The tearing parity modes can achieve significant growth rates as seen in the dispersion relation shown in Fig. 6, but are always subdominant to the ballooning-parity modes for the parameter regimes studied here. Table I also outlines the properties of the MTM, which is similar to the other electron modes, with the exception of its electromagnetic properties. The microtearing properties listed in Table I were identified for parameter regimes where microtearing is the dominant instability, as described in Ref. 24. The mode is sensitively dependent on β and comparatively unchanged in simulations where the electrostatic potential is artificially deleted from the linear operator. Moreover, it is associated with a large positive quasilinear electron EM flux component $(Q_e^{EM}/|Q_e^{ES}|)_{linear}$, whereas the other modes are characterized by small (and often negative) quasilinear magnetic fluxes.

Downloaded 07 Aug 2013 to 130.183.100.98. This article is copyrighted as indicated in the abstract. Reuse of AIP content is subject to the terms at: http://pop.aip.org/about/rights_and_permissions

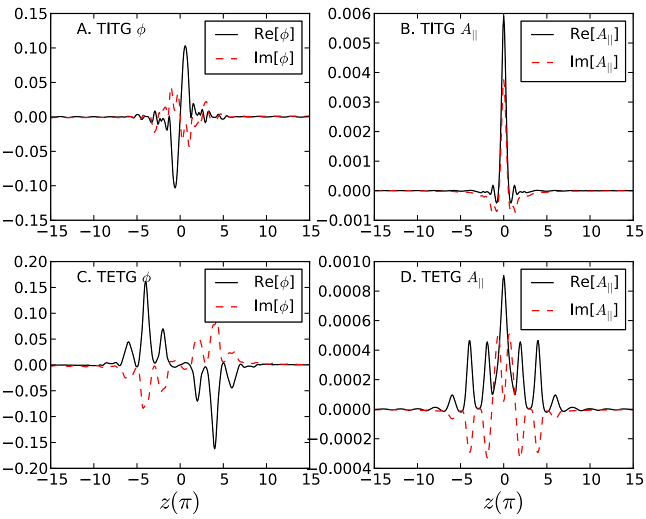

FIG. 5. Extended parallel mode structures of representative TITG ((A) and (B)) and the TETG modes ((C) and (D)) for $\beta = 0.003, k_y\rho_s = 0.2$, and centered at $k_x\rho_s = 0$.

For the CBC parameters considered here, an authentic MTM can be found deeper (i.e., more strongly damped) in the eigenmode spectrum. A direct eigenmode solver based on the SCALAPACK library was used to solve for the entire set of eigenmodes. The direct solver (which scales like N^3, where N is the total number of grid points) enforces a severe limit on the resolution, which can be achieved. As a result, we use a reduced resolution case (with seven k_x modes, and (16, 32, 8) grid points in the $(z, v_{||}, \mu)$ coordinates), which is somewhat under-resolved, but nonetheless offers some insight into the linear spectrum. The MTM can be identified, from among the thousands of modes produced by the direct solver, by its quasilinear EM flux $(Q_e^{EM}/|Q_e^{ES}|)_{linear}$, which is orders of magnitude larger than that of any other mode in the spectrum. For the parameters studied $(k_y\rho_s = 0.2, \beta = 0.003)$, the mode's $A_{||}$ structure is well resolved, but the Φ structure cannot be fully resolved with the seven k_x modes (fewer than in the nonlinear simulations), which can be achieved with the eigenvalue solver. The mode has a frequency $\omega = -0.98c_s/R$ and is robustly damped with a damping rate $\gamma = -0.43c_s/R$, although these values may change for better resolved simulations. Additional tests indicate that this mode has properties consistent with MTMs: The mode is sensitive to changes in the electron temperature gradient but not the ion temperature gradient, and it is fundamentally changed in the electrostatic limit but not when the electrostatic potential is artificially deleted.

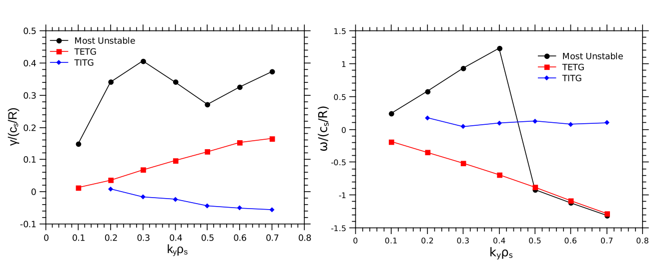

FIG. 6. Dispersion relations for the ITG/TEM (black circles), most unstable TETG (red squares), and most unstable TITG (blue diamonds) modes.

TABLE I. Summary of mode characteristics for several linear eigenmodes. The MTM is unique in its electromagnetic properties.

	ITG	TITG	ETG	TETG	MTM
Tearing parity		X		X	X
Frequency sign	+	+	−	−	−
R/L_{Ti} threshold	X	X			
R/L_{Te} threshold			X	X	X
β threshold					X
Strongly Φ dependent	X	X	X	X	
$\lvert Q_e^{EM}\rvert/\lvert Q_e^{ES}\rvert$	$\ll 1$	$\ll 1$	$\ll 1$	$\ll 1$	>1

In summary, three types of linear modes with tearing parity can be identified in the linear eigenmode spectrum: tearing-parity variants of conventional ITG and ETG modes, and a stable MTM which has properties consistent with the unstable MTMs described in the literature. Although the TITG and TETG modes can be unstable, we demonstrate below that several properties of the nonlinear tearing fluctuations and the resulting transport cannot be explained by the TITG and TETG modes, but are closely related to the authentic MTM. Moreover, we demonstrate that the EM transport is nonlinearly excited, eliminating the need for a linear instability mechanism.

V. CONNECTION BETWEEN NONLINEAR DYNAMICS AND MICROTEARING MODES

A. Comparison of linear modes with SVD modes

Having described the linear eigenmodes with tearing parity, we now examine in detail the properties of the nonlinear fluctuations, which produce the EM transport, and seek connections with the linear tearing-parity modes. To this end, we examine SVDs of the modified gyrocenter distribution function

$$g_{k_x^+,k_y}(z, v_{||}, \mu, t) = \sum_n g_{k_x^+,k_y}(z, v_{||}, \mu)_{||}^{(n)} h_{k_x^+,k_y}^{(n)}(t). \quad (7)$$

This procedure is identical to that described in Sec. III A for $A_{||}$, except that each column of the input matrix now additionally contains the $v_{||}$ and μ dependence of the distribution function. Note that the SVD modes produced by this decomposition have the same functional dependence as the distribution function produced when performing a linear calculation, i.e., they both have the same $(k_x^+, z, v_{||}, \mu)$ domain. As a result, many aspects of these SVD modes can be compared directly with the linear modes described in Sec. IV, notably, self consistent Φ and $A_{||}$ mode structures, and quasilinear fluxes. This SVD of the distribution function also facilitates a free-energy-based investigation of nonlinear excitation mechanisms, described in Sec. VI B.

We first examine the nonlinearly evolved distribution function for the $\beta = 0.003$ case at $k_y\rho_s = 0.2$, and centered at $k_x\rho_s = 0$ (with an extended mode structure consisting of nine k_x modes). An SVD mode decomposition of the form of Eq. (7) is constructed from this data set, and produces an $n = 1$ SVD mode that is very similar to the unstable ITG

Downloaded 07 Aug 2013 to 130.183.100.98. This article is copyrighted as indicated in the abstract. Reuse of AIP content is subject to the terms at: http://pop.aip.org/about/rights_and_permissions

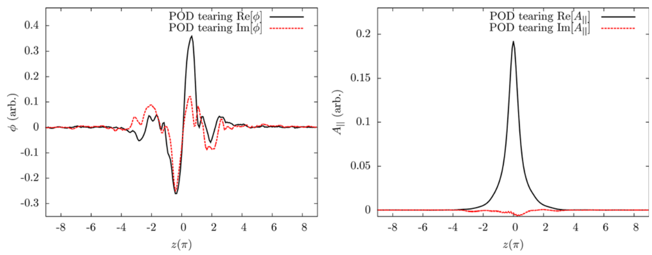

FIG. 7. Parallel mode structure of the tearing-parity mode constructed from an SVD of the gyrocenter distribution function at $\beta = 0.003, k_y\rho_s = 0.2$, and centered at $k_x\rho_s = 0$. The mode produces the dominant contribution to the outward electromagnetic heat flux at this wave number.

mode. In order to determine the SVD modes that are responsible for the magnetic stochasticity and associated transport, the electron EM heat flux was calculated for each mode. Although the SVD modes are not orthogonal for the heat flux operation, the orthogonality of the SVD time traces allows a time-averaged heat flux to be uniquely associated with each mode. The $n = 4$ SVD mode possesses tearing parity and additionally defines the dominant outward contribution to Q_e^{EM}; for this mode $Q_e^{EM}/(c_sP_0\rho_s^2/R^2) = 1.0$, compared with a total of $Q_e^{EM}/(c_sP_0\rho_s^2/R^2) = -6.3 \times 10^{-3}$ for all other subdominant ($n > 1$) modes combined. Thus the transport associated with this wave number can be completely described by the dominant ITG mode ($n = 1$) and the dominant tearing mode ($n = 4$). The mode structure for this tearing mode is shown in Fig. 7 and exhibits clearly dominant tearing parity with a (largely) symmetric $A_{||}$ and antisymmetric Φ. SVDs of extended mode structures at other wave numbers are similar, although in some cases two or more similar SVD modes produce significant contributions to the EM flux, and at $|k_x| > 0$, the parity of the mode structures is more strongly mixed.

Note that the Φ mode structure shown in Fig. 7 is well resolved with only a few k_x connections (i.e., a few multiples of π) in contrast with the MTMs described in Refs. 23–25. MTMs with limited mode structures similar to those described here have recently been identified in gyrokinetic simulations in other parameter regimes.[27,28]

The $A_{||}$ mode structure of the SVD mode is plotted along with the corresponding mode structures for the tearing-parity linear eigenmodes in Fig. 8; the SVD mode has a nearly identical mode structure to the linear MTM, whereas the distinctive features of the TITG and TETG modes are not observed. Other features of the modes also indicate a connection between the SVD mode and the linear MTM; as summarized in Table II, these modes have comparable values of quasilinear EM fluxes and the ratio of $A_{||}$ to Φ intensity, whereas the values for the TITG and TETG modes are orders of magnitude smaller. These observations are a strong indication that the fluctuations responsible for the magnetic stochasticity and transport are nonlinear manifestations of MTMs similar to those described in the literature.

B. Linear eigenmode projection

Additional insight can be gained by projecting the nonlinear distribution function onto a partial basis of linear eigenmodes. To this end, a nonlinear simulation was performed using

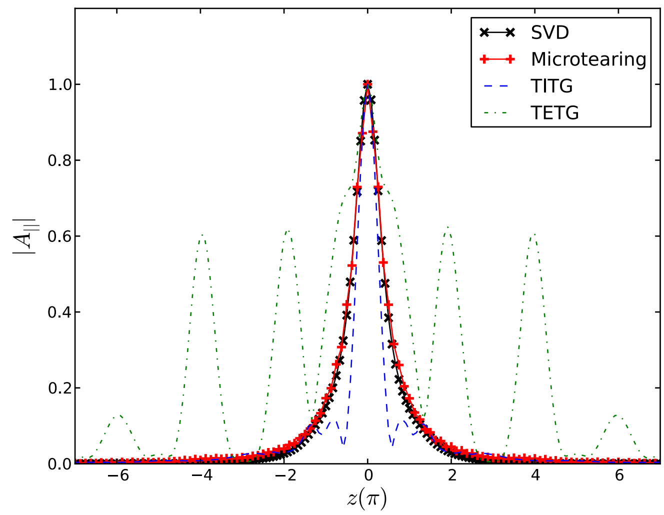

FIG. 8. Comparison of the $A_{||}$ mode structures for the SVD tearing-parity mode (black x's), the linear subdominant microtearing mode (red +'s), the TITG mode (blue dashed line), and the TETG mode (green dot-dashed line). The SVD mode clearly matches the microtearing mode structure but not the TITG or TETG modes.

parameters corresponding to those used to calculate the linear MTM described in Sec. IV. The distribution function for the extended mode structure at $k_y\rho_s = 0.2$ and centered at $k_x\rho_s = 0$ was projected onto a large set of orthogonalized eigenmodes.[36] The eigenmodes were orthogonalized using the Gram-Schmidt procedure starting with the ITG mode and the MTM, followed by a large subset of subdominant modes ordered by linear growth rate. The contribution of each mode to the EM heat transport was calculated and is shown in Fig. 9, where the eigenvalues are plotted in the complex plane representing the mode growth rates and frequencies, and the color weighting indicates the absolute value of the EM transport produced by each mode. The ITG mode is associated with a large negative value, and the subdominant tearing mode (with $\gamma = -0.43c_s/R$ and $\omega = -0.98c_s/R$) produces a significant positive value. All other modes produce only small contributions to the EM transport. Note that the MTM does not achieve an extraordinarily high *amplitude* in relation to the other subdominant modes, but rather only a large contribution to the EM heat flux due to its large quasilinear Q_e^{EM}.

It should be noted that the modes cannot be orthogonalized for the EM heat flux operator, which is not a valid scalar product (because it can violate the condition $\langle v, v\rangle > 0$ when $v \neq 0$). For this reason, and because of the resolution constraints enforced by the direct eigenmode solver, this eigenmode projection should be considered as a qualitative rather than quantitative description of the transport dynamics.

TABLE II. Summary of mode properties connecting the SVD tearing mode and the linear MTM, and distinguishing them from the TITG and TETG modes.

	TITG	TETG	MTM	SVD
$Q_e^{EM}/\lvert Q_i^{ES}\rvert$	4.8×10^{-3}	-0.13	730	330
$\int A_{\parallel}^2 dz/\int \Phi^2 dz$	1.3×10^{-3}	2.8×10^{-5}	0.10	0.16

Downloaded 07 Aug 2013 to 130.183.100.98. This article is copyrighted as indicated in the abstract. Reuse of AIP content is subject to the terms at: http://pop.aip.org/about/rights_and_permissions

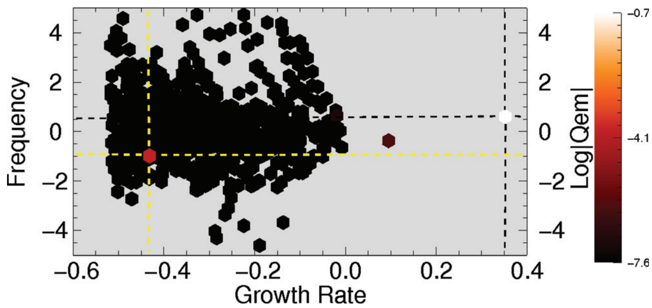

FIG. 9. A subset of the linear eigenvalues plotted in the complex plane defined by the growth rate and frequency at $\beta = 0.003, k_y\rho_s = 0.2$, and centered at $k_x\rho_s = 0$. The color weighting is produced by projecting the nonlinearly evolved distribution function onto this subset of orthogonalized eigenmodes and calculating the time-averaged absolute value of the electron electromagnetic heat flux associated with each mode. The ITG mode produces a significant negative flux, and the microtearing mode produces a significant outward flux.

C. Microtearing considerations

The connection between the MTM and the EM transport studied here motivates an investigation of certain physical and numerical properties to which microtearing is known to be sensitive. Microtearing physics can be extremely demanding to resolve numerically, requiring both very small radial scales (i.e., a very extended mode structure) in order to resolve the electrostatic potential fluctuations and current layers, and large radial box sizes to resolve the $A_{||}$ fluctuations. For this reason, nonlinear simulations where microtearing is the dominant instability have only become accessible in the last few years.[24,25] Unfortunately, linear convergence tests directly examining the resolution requirements of the subdominant MTM are not possible because of the scaling properties of the direct eigenmode solver described in Sec. IV. However, as shown in Fig. 7, the microtearing mode structure extracted from the nonlinear simulations is sufficiently resolved. Moreover, microtearing modes with similar mode structures (i.e., requiring only a few k_x connections) have recently been observed in other scenarios.[27,28]

Additionally, nonlinear resolution tests were performed (in addition to the thorough convergence tests described in Ref. 14). A simulation at $\beta = 0.003$ using increased parallel and velocity-space resolution ((48, 64, 16) grid points in the $(z, v_{||}, \mu)$ coordinates) and two simulations (at $\beta = 0.003$ and 0.006) with increased radial resolution (using 392 k_x modes resolving up to $k_{xmax}\rho_s = 11.9$) show no significant change in transport levels. Note that the radial hyperdiffusion is of the form $c(k_x/k_{xmax})^4$, where c is a user-defined coefficient, so that when the resolution is increased, the operator only becomes active at correspondingly higher wave numbers.

Microtearing modes are also sensitive to collisions, which are neglected in the CBC β scan but are an integral part of microtearing physics. The dependence of microtearing modes on collisionality is non-trivial; collisions can be either stabilizing or destabilizing depending on the parameter regime.[26–28] Nonlinear collisionality scans were performed for the $\beta = 0.003, 0.006$ cases covering the regime $\nu R/c_s \ll 1$ to $\nu R/c_s \approx 1$. At $\nu R/c_s \ll 1$, the EM transport is similar to the collisionless cases. As ν increases, the ES transport decreases consistent with the corresponding decrease of the ITG growth rate. The EM transport also decreases, but at a much faster rate than the ES transport, as shown in Fig. 10. In both scans, the electron EM transport is strongly suppressed in relation to the ES transport as $\nu R/c_s \to 1$. It is unknown whether these features are related to a direct effect on the microtearing modes, an indirect effect on the nonlinear excitation mechanism, or simply the properties of heat transport in a stochastic magnetic field.

VI. NONLINEAR EXCITATION MECHANISM

A. Nonlinear time scales

Having demonstrated a connection with the linear microtearing mode, we now seek to identify an excitation mechanism. The electron EM transport shows distinct signatures of nonlinear excitation. Fig. 11(A) shows the time traces for the electron EM heat flux along with the electrostatic channels for the $\beta = 0.007$ case. The ion and electron ES transport channels are both produced by the ITG mode, and their time traces are highly correlated; the nonlinear amplitudes fluctuate in phase with each other and differ only by their relative amplitude, which is related to the properties of the linear ITG mode. In the early time linear growth phase (shown in Fig. 11(B)), the ES channels grow at approximately the rate that would be expected from the linear growth rate of the ITG mode (note that growth rates shown here are twice the corresponding linear growth rates since the flux is a quadratic quantity). The EM transport begins growing at a later time than the ES transport. Moreover, in contrast to the ES transport, the EM transport exhibits no smooth exponential growth, but rather a general trend of growth at approximately twice the rate of the ES channels, punctuated by brief sharp increases. Both the general trend

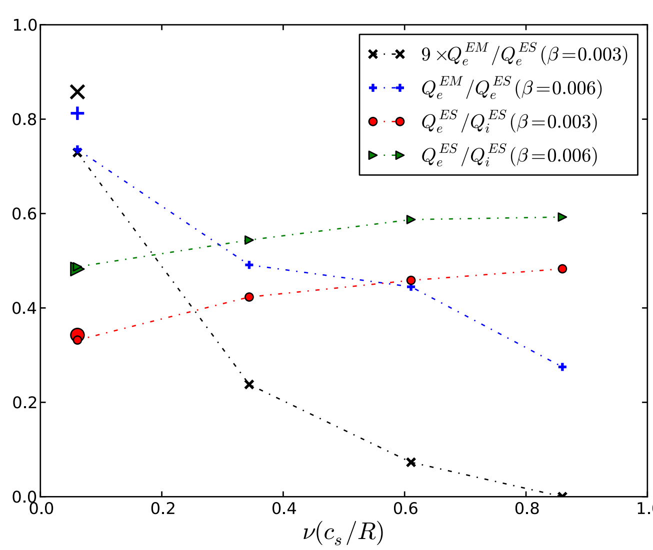

FIG. 10. The ratio Q_e^{EM}/Q_e^{ES} over a scan in collisionality for the $\beta = 0.003$ case (black x's) and the $\beta = 0.006$ case (blue +'s), and the ratio Q_e^{ES}/Q_i^{ES} for the same β cases (red circles and green triangles, respectively). The EM transport is suppressed as collisionality increases. The larger free-standing symbols at the lowest collisionality point represent velocity space resolution tests with (96,16) and (48,16) grid points in $(v_{||}, \mu)$ for the $\beta = 0.003$ and $\beta = 0.006$ cases, respectively.

Downloaded 07 Aug 2013 to 130.183.100.98. This article is copyrighted as indicated in the abstract. Reuse of AIP content is subject to the terms at: http://pop.aip.org/about/rights_and_permissions

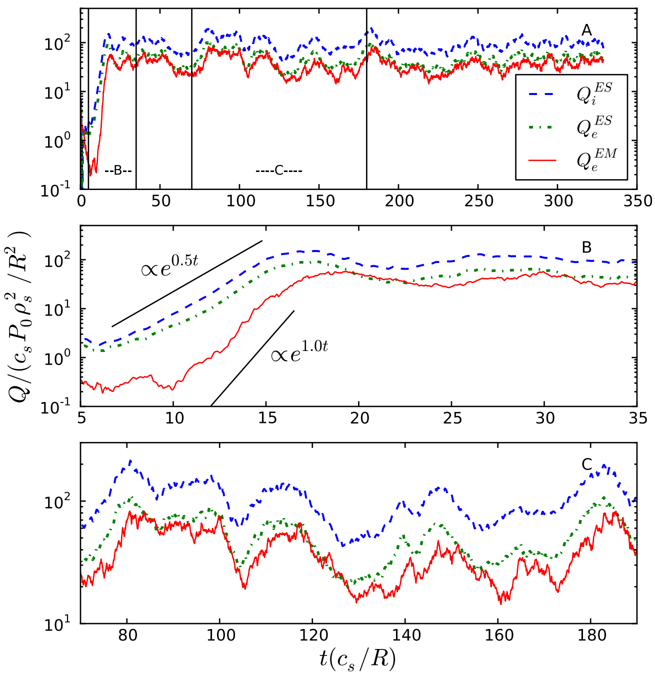

FIG. 11. Time traces of the ion electrostatic (blue dashed line), electron electrostatic (green dotted-dashed line), and electron electromagnetic (red solid line) for the $\beta = 0.007$ case. The electrostatic transport channels are in phase and are associated with the same time scales as the linear growth rates. The electromagnetic flux lags the electrostatic channels and is characterized by time scales faster than the linear time scales, suggesting a nonlinear excitation mechanism.

($\gamma R/c_s \approx 1$) and the bursts ($\gamma R/c_s \gg 1$) are much larger than any linear growth rates in the system, indicating a nonlinear excitation mechanism.

In the saturated phase shown in Fig. 11(C), these relative time scales are maintained. A probability distribution function (PDF) of the instantaneous growth rates $(1/Q)\,\partial Q/\partial t$ shows that the ES growth rates are characteristic of the linear growth time scales, while the instantaneous EM growth rates are characterized by time scales, which are much larger than the ES growth rates. Additionally, the ES channels continue to fluctuate in phase in the saturated state. In contrast, the EM channel follows the trends of the ES channels, but typically with a time lag. The cross correlation function $C(\tau) = \int Q_e^{ES}(t)\, Q_e^{EM}(t+\tau)\, dt$ indicates that the two signals are most strongly correlated at $\tau c_s/R \simeq 2$.

These basic properties are observed, with some variation, throughout the β scan and also in the TEM β scan described in Ref. 15.

B. Nonlinear excitation through coupling with zonal wave numbers

In order to identify the relevant nonlinear coupling mechanisms, we construct an SVD of the gyrocenter distribution function from a GENE simulation and examine the energetics of the tearing fluctuations. We examine in detail the SVD microtearing mode described in Sec. V A ($k_y\rho_s = 0.2, k_x\rho_s = 0$ for the $\beta = 0.003$ case). In order to study the excitation mechanism of this mode, we construct nonlinear energy transfer functions.[49,50] The free energy[51] is defined as

$$E_{\mathbf{k}} = \sum_j \int dz\, dv_{||}\, d\mu\, T_{j0}/F_{j0}(g_{j\mathbf{k}} + q_j F_{j0}/T_{j0}\chi_{j\mathbf{k}})^* g_{j\mathbf{k}}, \quad (8)$$

where j denotes the particle species, q_j is particle charge, F_{j0} is the background Maxwellian distribution function, $\chi_j = \bar{\Phi}_j + v_{Tj} v_{||} \bar{A}_{||j}$, where the overbar denotes a gyroaverage, and v_{Tj} is the particle thermal velocity. Normalization is as described in Ref. 52. The corresponding energy evolution equation is

$$\partial_t E_{\mathbf{k}} = \mathcal{L}[g_{\mathbf{k}}, g_{\mathbf{k}}] + \sum_{\mathbf{k}'} \mathcal{N}_{\mathbf{k},\mathbf{k}'}[g_{\mathbf{k}}, g_{\mathbf{k}'}, g_{\mathbf{k}-\mathbf{k}'}] + c.c., \quad (9)$$

where $\mathcal{L}$ includes the linear gyrokinetic operator, $c.c.$ denotes the complex conjugate, and the nonlinear energy transfer function $\mathcal{N}$ is defined as

$$\mathcal{N}_{\mathbf{k},\mathbf{k}'} = \sum_j \int dz\, dv_{||}\, d\mu\, (k_x' k_y - k_x k_y') \times [q_j \chi^*_{j\mathbf{k}} \chi_{j\mathbf{k}'} g_{j(\mathbf{k}-\mathbf{k}')} - T_{j0}/F_{j0} g^*_{j\mathbf{k}} \chi_{j(\mathbf{k}-\mathbf{k}')} g_{j\mathbf{k}'}]. \quad (10)$$

The latter represents the energy transferred conservatively between the wave numbers (k_x, k_y) and (k_x', k_y'), as evidenced by the property $\mathcal{N}_{\mathbf{k},\mathbf{k}'} = -\mathcal{N}_{\mathbf{k}',\mathbf{k}}$. This energy equation, however, defines the nonlinear energy transfer function for all fluctuations at a given wave number; a refinement is necessary to examine the energetics of the tearing mode of interest: $\partial_t E_{\mathbf{k}}^{(tear)} = \mathcal{L}[g_{\mathbf{k}}^{(tear)}, g_{\mathbf{k}}] + \sum_{\mathbf{k}'} \mathcal{N}_{\mathbf{k},\mathbf{k}'}[g_{\mathbf{k}}^{(tear)}, g_{\mathbf{k}'}, g_{\mathbf{k}-\mathbf{k}'}]$, where $g^{(tear)}$ represents the SVD tearing mode described above, and the LHS represents the evolution of the tearing mode energy due to the orthogonality of the SVD modes.

It is observed that the nonlinear energy transfer for the tearing mode is dominated by energy injected *into* the mode from wave numbers at the same k_y and $|k_x| > 0$, and energy transferred *out* of the mode into zonal wave numbers ($k_y = 0$). Note that both of these energy transfer channels represent coupling with zonal modes, i.e., either $k_y' = 0$ or $k_y'' \equiv k_y - k_y' = 0$. A closer examination shows that the energetics of the mode is dominated by the imbalance between this energy transfer as demonstrated in Fig. 12. The free energy of the tearing mode is plotted along with the total nonlinear drive for a time period in the saturated nonlinear phase. The linear contribution (not shown in Fig. 12) also occasionally plays a role but is much smaller than the nonlinear term, which dominates both the drive and saturation of the mode; in general, the free energy increases when the nonlinear drive is positive and decreases when the nonlinear drive is negative. Also shown in Fig. 12 is the component of the nonlinear drive defined by the subset of wave numbers representing zonal coupling: $k_y'\rho_s = 0.2$ and $k_y'\rho_s = 0$. This subset closely tracks the total nonlinear drive and captures the major trends in the energy balance. We thus have the unique situation where the saturation mechanism for the driving ITG instability in turn catalyzes a significant additional transport channel. It is interesting to note that in two-dimensional fluid models of plasma microturbulence, zonal flows have been identified as the main mechanism for damped eigenmode excitation.[53]

Downloaded 07 Aug 2013 to 130.183.100.98. This article is copyrighted as indicated in the abstract. Reuse of AIP content is subject to the terms at: http://pop.aip.org/about/rights_and_permissions

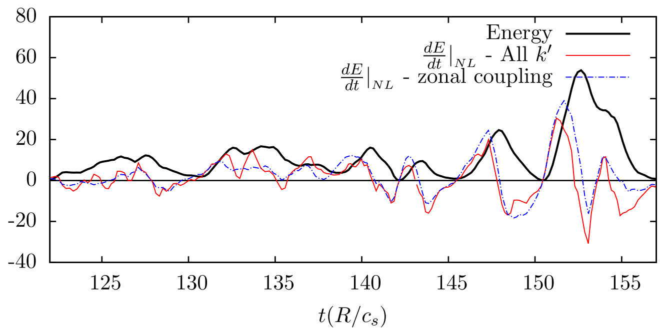

FIG. 12. The free energy in the SVD tearing mode (solid black line) at $\beta = 0.003, k_y\rho_s = 0.2$, and centered at $k_x\rho_s = 0$, along with the total nonlinear drive (gray line–red online) and the nonlinear drive defined by coupling with zonal wave numbers (dashed line–blue online), plotted over a time segment of the nonlinear saturated state. The energetics of the tearing mode is dominated by the nonlinear drive which consists largely of the zonal coupling. Reprinted with permission from D. R. Hatch *et al.*, Phys. Rev. Lett. **108**, 235002 (2012). Copyright 2012 the American Physical Society.

The excitation mechanism outlined above is observed for a wide range of wave numbers (a k_y scan at $k_x = 0$ and a k_x scan at $k_y\rho_s = 0.2$). For $|k_x| > 0$ wave numbers, an additional mechanism is sometimes observed. For some tearing SVD modes, the linear term in the energy balance drives the mode, and the nonlinear term balances the linear drive. This is interpreted as a manifestation of sub-critical instability since no unstable tearing-parity modes with significant quasilinear EM transport are observed in the linear spectra at these wave numbers.

The analysis presented above cannot distinguish between zonal flows and GAMs, which are both $k_y = 0$ fluctuations. This distinction may be important when taking into account parity considerations of the coupling mechanism. Zonal flows are uniform in the z direction, while GAMs have an odd parallel component. Thus, it may be expected that a GAM would couple more effectively with a ballooning parity ITG mode to drive tearing-parity fluctuations. However, coupling between zonal flows and ITG modes is also possible when considering the odd component of $|k_x| > 0$ ITG modes. Neither zonal flows nor GAMs can be excluded as a contributing factor in the nonlinear excitation mechanism.

VII. TRANSPORT MODELING

The scenario described in this paper states that a significant component of the heat transport is not directly attributable to the driving instabilities. Such dynamics cannot be captured by quasilinear theory. Nonetheless, the EM transport channel is intimately connected to the ITG drive through the nonlinear excitation mechanism; the same mechanism that sets the ES transport levels (coupling with zonal modes) is also responsible for the excitation of the EM transport channel. It is thus plausible that the EM transport could be modeled in relation to the ES transport. Such a description would be useful as a tool for reduced transport modeling and also provide some expectations of how EM transport behaves in a broader parameter regime.

In Refs. 8 and 14, it is shown that the electron EM heat diffusivity χ_e^{EM} is proportional to β^2 times the ES diffusivity $\chi_{\rm ES} = \chi_i^{ES} + \chi_e^{ES}$. This estimate can be refined by including a quasilinear correction, which accounts for the contribution of the most unstable mode, as described in Ref. 8. These results motivate a simple model for the EM heat diffusivity

$$\chi_e^{\rm EM} \sim \sigma(\beta/\beta_{\rm crit})^2\chi_{\rm ES} + \chi_e^{ES}(\chi_e^{EM}/\chi_e^{ES})_{MU}\,, \qquad (11)$$

where $\beta_{\rm crit}$ is the KBM threshold (this normalization to $\beta_{\rm crit}$ is used in Ref. 54), MU denotes that these quantities are taken from the most unstable linear eigenmode, and σ is an order-unity constant that is expected to depend on such things as the collisionality, the relative effectiveness of the nonlinear excitation mechanism described in Sec. VI, and the parallel heat diffusivity $\chi_{e||} \approx q_0 R(T_e/m_e)^{1/2}$ (the parallel heat diffusivity can be used to relate χ_e^{EM} to the magnetic fluctuation amplitude[14,45]). The second term on the RHS of Eq. (11) describes the quasilinear EM heat diffusivity expected from the most unstable eigenmode. The first term on the RHS of Eq. (11) describes the component of the transport associated with the microtearing fluctuations and is plotted for both the CBC and TEM β scans in Fig. 13, where the values $\sigma = (0.92, 0.24)$ have been selected for the (CBC and TEM) scans, respectively. The quasilinear correction significantly improves the model at low β for the CBC scan,[8] but not for the TEM scan.

Note that the normalization to $\beta_{\rm crit}$ indicates that this β^2 proportionality factor will typically be smaller—often much smaller—than unity. Some conclusions can be drawn about the σ factor by examining the database of nonlinear EM gyrokinetic simulations described in Ref. 54. The database comprises thirty nonlinear EM simulations consisting of variations in gradient scale lengths $(R/L_n = [0.37, 3.0], R/L_{Te} = [0, 6.9], R/L_{Ti} = [0, 10.4]), \beta = [0.001, 0.02], q_0 = [1.4, 3.7]$, and $\hat{s} = [0.57, 2.5]$ representative of typical core parameters. Simulations modeling ASDEX upgrade and JET discharges using experimental profiles and equilibria are also included. It is found that the value $\sigma = 1$ is an upper bound for almost all simulations in the database (excluding MTM driven turbulence). Several simulations with low values of $(\beta/\beta_{\rm crit})^2\chi_{\rm ES}$ exhibit negative EM diffusivities as would be expected from the quasilinear term in Eq. (11).

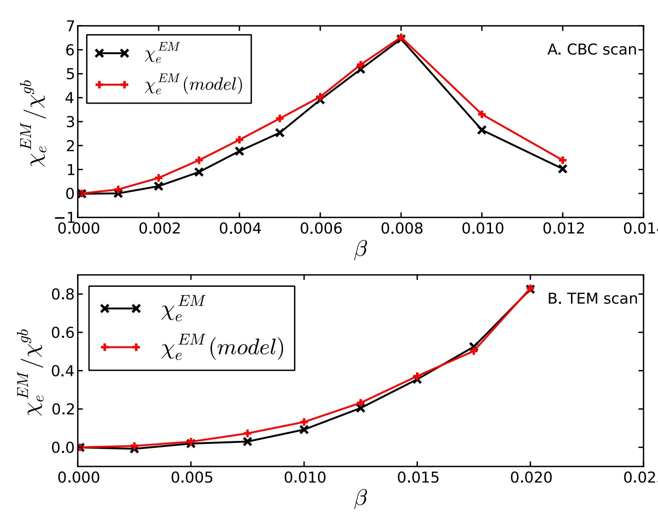

FIG. 13. The electron electromagnetic heat diffusivity (black x's) plotted over the β scan and the same quantity produced from the first term on the rhs of Eq. (11) (red +'s), for the CBC case (A) and the TEM case (B). Values of $\sigma = (0.92, 0.24)$ were used for the (CBC, TEM) cases, respectively.

Downloaded 07 Aug 2013 to 130.183.100.98. This article is copyrighted as indicated in the abstract. Reuse of AIP content is subject to the terms at: http://pop.aip.org/about/rights_and_permissions

These results suggest that high-β ITG/TEM transport will not produce drastically high levels of electromagnetic heat flux for typical core parameters. The effective result of EM effects on ITG/TEM driven transport is a shift away from ion heat transport to processes where the transport is more heavily driven in the electron channel, with gradients still constrained by a β limit (KBM, or possibly the scenario described in Ref. 43).

VIII. SUMMARY AND CONCLUSIONS

This study has provided a detailed examination of the mechanisms whereby magnetic stochasticity and transport develop in electromagnetic ITG-driven turbulence. Two possible sources of tearing-parity fluctuations were considered, namely linear eigenmodes with tearing parity and ITG modes at $|k_x| > 0$. The magnetic fluctuations from nonlinear simulations were decomposed according to parity considerations into predominantly ballooning parity fluctuations corresponding to the ITG modes, and predominantly tearing-parity fluctuations. It was shown that the latter are responsible for the magnetic stochasticity, eliminating the ITG mode as the direct cause of the EM effects. The EM heat transport is a superposition of an inward component associated with the ITG modes and an outward component associated with the tearing fluctuations; the outward component scales like $\beta^2 Q^{ES}$ and eventually dominates as β increases.

The linear eigenmodes that have tearing-parity were classified and described. Three types of tearing-parity modes were identified; TITG and TETG modes are similar to conventional ITG and ETG modes with the exception of the mode parity and may be unstable for the parameter regimes studied here. Additionally, a stable microtearing mode was found in the linear spectrum. SVD decompositions of the nonlinearly evolved distribution function produce modes that most efficiently describe the nonlinear fluctuations and can be compared with the linear eigenmodes. These decompositions reveal tearing-parity modes, which are responsible for the EM heat flux and have characteristics (including parallel mode structures, quasilinear EM fluxes, and the ratio of $A_{||}$ to Φ) that are very similar to linear microtearing modes and dissimilar to the TITG and TETG modes. It was concluded that microtearing modes are responsible for the magnetic stochasticity and associated heat transport. This is further substantiated by a projection of the nonlinearly evolved distribution function onto a partial basis of linear eigenmodes, which demonstrates significant contributions to the outward EM transport only from the subdominant microtearing mode.

The EM heat flux shows signatures of nonlinear excitation, being associated with growth time scales (in both the earlier linear and later saturated phases) much larger than the linear growth rates in the system. An examination of nonlinear energy transfer functions revealed that the predominant excitation mechanism for the microtearing modes is coupling with zonal modes (modes at $k_y = 0$).

A simple formula was presented relating EM transport to ES transport, and it was tentatively concluded that ITG/TEM driven EM transport will not produce drastically high transport levels for typical core parameters.

In summary, this work explains many of the features of EM microturbulence discovered in recent gyrokinetic studies and may offer a paradigm, which can be examined in a broader range of parameter regimes, for how magnetic fluctuations develop in turbulence driven by instabilities that are not intrinsically electromagnetic. This paradigm may shed light on the various β scalings for confinement reported experimentally, and ultimately offer insight into how EM effects on transport may be manifest in future devices such as ITER.

ACKNOWLEDGMENTS

This work was carried out using the HELIOS supercomputer system at the International Fusion Energy Research Centre, Aomori, Japan, under the Broader Approach collaboration between Euratom and Japan, implemented by Fusion for Energy and JAEA. Resources were also used at the Oak Ridge Leadership Computing Facility at the Oak Ridge National Laboratory, which is supported by the Office of Science of the U.S. Department of Energy under Contract No. DE-AC05-00OR22725. Funding was received from the European Research Council under the European Union's Seventh Framework Programme (FP7/2007-2013)/ERC Grant Agreement No. 277870. The authors wish to acknowledge useful conversations with E. Wang and W. Dorland.

[1]C. C. Petty, Phys. Plasmas **15**, 080501 (2008).
[2]F. Jenko, W. Dorland, M. Kotschenreuther, and B. N. Rogers, Phys. Plasmas **7**, 1904 (2000).
[3]S. E. Parker, W. W. Lee, and R. A. Santoro, Phys. Rev. Lett. **71**, 2042 (1993).
[4]A. M. Dimits, G. Bateman, M. A. Beer, B. I. Cohen, W. Dorland, G. W. Hammett, C. Kim, J. E. Kinsey, M. Kotschenreuther, A. H. Kritz, L. L. Lao, J. Mandrekas, W. M. Nevins, S. E. Parker, A. J. Redd, D. E. Shumaker, R. Sydora, and J. Weiland, Phys. Plasmas **7**, 969 (2000).
[5]H. Nordman, J. Weiland, and A. Jarmén, Nucl. Fusion **30**, 983 (1990).
[6]T. Dannert and F. Jenko, Phys. Plasmas **12**, 072309 (2005).
[7]D. R. Ernst, J. Lang, W. M. Nevins, M. Hoffman, Y. Chen, W. Dorland, and S. Parker, Phys. Plasmas **16**, 055906 (2009).
[8]D. R. Hatch, M. J. Pueschel, F. Jenko, W. M. Nevins, P. W. Terry, and H. Doerk, Phys. Rev. Lett. **108**, 235002 (2012).
[9]F. Jenko and W. Dorland, Plasma Phys. Controlled Fusion **43**, A141 (2001).
[10]R. D. Sydora, Phys. Plasmas **8**, 1929 (2001).
[11]Y. Chen, S. E. Parker, B. I. Cohen, A. M. Dimits, W. M. Nevins, D. Shumaker, V. K. Decyk, and J. N. Leboeuf, Nucl. Fusion **43**, 1121 (2003).
[12]S. E. Parker, Y. Chen, W. Wan, B. I. Cohen, and W. M. Nevins, Phys. Plasmas **11**, 2594 (2004).
[13]J. Candy, Phys. Plasmas **12**, 072307 (2005).
[14]M. J. Pueschel, M. Kammerer, and F. Jenko, Phys. Plasmas **15**, 102310 (2008).
[15]M. J. Pueschel and F. Jenko, Phys. Plasmas **17**, 062307 (2010).
[16]R. E. Waltz, Phys. Plasmas **17**, 072501 (2010).
[17]W. M. Nevins, E. Wang, and J. Candy, Phys. Rev. Lett. **106**, 065003 (2011).
[18]E. Wang, W. M. Nevins, J. Candy, D. Hatch, P. Terry, and W. Guttenfelder, Phys. Plasmas **18**, 056111 (2011).
[19]J. F. Drake and Y. C. Lee, Phys. Rev. Lett. **39**, 453 (1977).
[20]L. Chen, P. H. Rutherford, and W. M. Tang, Phys. Rev. Lett. **39**, 460 (1977).
[21]J. D. Callen, Phys. Rev. Lett. **39**, 1540 (1977).
[22]J. W. Connor, S. C. Cowley, and R. J. Hastie, Plasma Phys. Controlled Fusion **32**, 799 (1990).
[23]D. J. Applegate, C. M. Roach, J. W. Connor, S. C. Cowley, W. Dorland, R. J. Hastie, and N. Joiner, Plasma Phys. Controlled Fusion **49**, 1113 (2007).

Downloaded 07 Aug 2013 to 130.183.100.98. This article is copyrighted as indicated in the abstract. Reuse of AIP content is subject to the terms at: http://pop.aip.org/about/rights_and_permissions

[24]H. Doerk, F. Jenko, M. J. Pueschel, and D. R. Hatch, Phys. Rev. Lett. **106**, 155003 (2011).
[25]W. Guttenfelder, J. Candy, S. M. Kaye, W. M. Nevins, E. Wang, R. E. Bell, G. W. Hammett, B. P. LeBlanc, D. R. Mikkelsen, and H. Yuh, Phys. Rev. Lett. **106**, 155004 (2011).
[26]H. Doerk, F. Jenko, T. Görler, D. Told, M. J. Pueschel, and D. R. Hatch, Phys. Plasmas **19**, 055907 (2012).
[27]W. Guttenfelder, J. Candy, S. M. Kaye, W. M. Nevins, E. Wang, J. Zhang, R. E. Bell, N. A. Crocker, G. W. Hammett, B. P. LeBlanc, D. R. Mikkelsen, Y. Ren, and H. Yuh, Phys. Plasmas **19**, 056119 (2012).
[28]D. Dickinson, C. M. Roach, S. Saarelma, R. Scannell, A. Kirk, and H. R. Wilson, "Microtearing modes at the top of the pedestal," Plasma Phys. Controlled Fusion (submitted).
[29]D. Told, F. Jenko, P. Xanthopoulos, L. D. Horton, E. Wolfrum, and ASDEX Upgrade Team, Phys. Plasmas **15**(10), 102306 (2008).
[30]L. Vermare, C. Angioni, A. Bottino, A. G. Peeters, and ASDEX Upgrade Team, J. Phys. Conf. Ser. **123**(1), 012040 (2008).
[31]P. H. Diamond, S.-I. Itoh, K. Itoh, and T. S. Hahm, Plasma Phys. Controlled Fusion **47**, R35 (2005).
[32]P. W. Terry, D. A. Baver, and S. Gupta, Phys. Plasmas **13**, 022307 (2006).
[33]J.-H. Kim and P. W. Terry, Phys. Plasmas **17**, 112306 (2010).
[34]K. Makwana, P. W. Terry, J.-H. Kim, and D. R. Hatch, Phys. Plasmas **18**, 012302 (2011).
[35]D. R. Hatch, P. W. Terry, F. Jenko, F. Merz, and W. M. Nevins, Phys. Rev. Lett. **106**, 115003 (2011).
[36]D. R. Hatch, P. W. Terry, F. Jenko, F. Merz, M. J. Pueschel, W. Nevins, and E. Wang, Phys. Plasmas **18**, 055706 (2011).
[37]F. Merz and F. Jenko, Nucl. Fusion **50**, 054005 (2010).
[38]W. Horton, B. G. Hong, and W. M. Tang, Phys. Fluids **31**, 2971 (1988).
[39]W. M. Nevins, J. Candy, S. Cowley, T. Dannert, A. Dimits, W. Dorland, C. Estrada-Mila, G. W. Hammett, F. Jenko, M. J. Pueschel, and D. E. Shumaker, Phys. Plasmas **13**, 122306 (2006).
[40]M. A. Beer, S. C. Cowley, and G. W. Hammett, Phys. Plasmas **2**, 2687 (1995).
[41]M. J. Pueschel, T. Dannert, and F. Jenko, Comput. Phys. Commun. **181**, 1428 (2010).
[42]A. Arakawa, J. Comput. Phys. **135**, 103 (1997).
[43]M. J. Pueschel, P. W. Terry, F. Jenko, D. R. Hatch, W. M. Nevins, T. Görler, and D. Told, "Extreme heat fluxes in gyrokinetic simulations: A new critical beta," Phys. Rev. Lett. (submitted).
[44]G. H. Golub and C. F. Van Loan, *Matrix Computations*, 2nd ed. (The Johns Hopkins University Press, Baltimore and London, 1989), p. 71.
[45]A. B. Rechester and M. N. Rosenbluth, Phys. Rev. Lett. **40**, 38 (1978).
[46]J. E. Roman, M. Kammerer, F. Merz, and F. Jenko, Parallel Comput. **36**, 339 (2010).
[47]F. Merz, C. Kowitz, E. Romero, J. E. Roman, and F. Jenko, Comput. Phys. Commun. **183**, 922 (2012).
[48]L. S. Blackford, J. Choi, A. Cleary, E. D'Azevedo, J. Demmel, I. Dhillon, J. Dongarra, S. Hammarling, G. Henry, A. Petitet, K. Stanley, D. Walker, and R. C. Whaley, ScaLAPACK Users' Guide, Society for Industrial and Applied Mathematics, Philadelphia, PA, 1997.
[49]C. Holland, P. H. Diamond, S. Champeaux, E. Kim, O. Gurcan, M. N. Rosenbluth, G. R. Tynan, N. Crocker, W. Nevins, and J. Candy, Nucl. Fusion **43**, 761 (2003).
[50]M. Nakata, T.-H. Watanabe, and H. Sugama, Phys. Plasmas **19**, 022303 (2012).
[51]A. Bañón Navarro, P. Morel, M. Albrecht-Marc, D. Carati, F. Merz, T. Görler, and F. Jenko, Phys. Plasmas **18**, 092303 (2011).
[52]T. Görler, X. Lapillonne, S. Brunner, T. Dannert, F. Jenko, F. Merz, and D. Told, J. Comput. Phys. **230**, 7053 (2011).
[53]K. D. Makwana, P. W. Terry, and J.-H. Kim, Phys. Plasmas **19**, 062310 (2012).
[54]M. J. Pueschel, F. Jenko, M. Schneller, T. Hauff, S. Günter, and G. Tardini, Nucl. Fusion **52**, 103018 (2012).

Downloaded 07 Aug 2013 to 130.183.100.98. This article is copyrighted as indicated in the abstract. Reuse of AIP content is subject to the terms at: http://pop.aip.org/about/rights_and_permissions